A High-Throughput Technique for Unidirectional Critical Current Density Testing of Solid Electrolyte Materials

*Danielle M. Gendron, Alireza Torabi, Mathew Wanees, Macwin Savio Dsouza, Ben Feddersen, Tim Holme**

Danielle Gendron, Alireza Torabi, Mathew Wanees, Macwin Savio Dsouza, Ben Feddersen, Tim Holme
QuantumScape Battery, Inc., San Jose, California 95110, USA
th+jes@quantumscape.com

Ben Feddersen
University of Hamburg, D-20148 Hamburg, Germany

Abstract

Work on solid electrolytes for rechargeable lithium-based batteries is motivated by the potential benefits of lithium-metal anodes for a variety of applications, including electric vehicles. Dendrite formation has been the key challenge preventing commercialization of rechargeable lithium-metal batteries, so establishing, validating, and improving the dendrite resistance of electrolytes is a key enabler of progress in the field. Typical symmetric cycling tests of Li-Li cells introduce operational and theoretical limitations which compromise the data produced and the conclusions which can be drawn from such testing. A high-throughput technique for unidirectional critical current density testing is presented which has allowed the development of a solid electrolyte capable of withstanding current densities of at least 300 mA cm^{-2}. The theoretical and empirical basis for this testing methodology is outlined, results are presented and analyzed, and best practices for critical current density testing of solid electrolyte materials are proposed.

1. Introduction

Replacing the graphite anodes of conventional lithium-ion batteries with lithium metal presents an opportunity to substantially increase the capacity of the negative electrode and, as a consequence, the energy density of the overall cell.[1][2] Work on solid electrolyte (SE) materials is motivated by the many practical challenges of lithium metal, in particular the tendency to form dendrites that cause cell failure and present serious safety risks in systems using liquid electrolytes.[3]–[6]

To demonstrate the level of dendrite resistance offered by any given SE, the critical current density (CCD) of the SE material must be established with precision.[7]–[9] While it should be emphasized that CCD measurement is not a replacement for full-cell testing across a wide range of conditions, improved performance of the SE in a component-level test is likely, all else being equal, to yield benefits at the full-cell level. A typical test of CCD is a Li-Li symmetric cycling test, whereby the lithium is alternatingly stripped and plated from Li-metal reservoirs on either side of the SE, and each cycle is stepped to a higher current density.[10]–[12] The current density at which the symmetric cell is observed to short is then taken to be the critical current density. Because of the importance of CCD, improving SE CCD has been a major focus of SE materials research.[12]–[21]

CCD measurement is frequently performed in Li-Li symmetric cells; while it is possible to run a CCD test using full cells, using a Li-ion battery cathode material as the Li source adds complexity due to the varying cell voltage, making identification of the short based on the voltage response more problematic than in Li-Li cells. Furthermore, most cathodes would reach limiting currents before achieving very high current densities (above 100 mA cm^{-2}). For these

reasons, the measurement is performed in a Li|SE|Li configuration; elsewhere in the literature, the Li electrodes consist of Li foil,[22] but the electrodes may also be produced by physical vapor deposition or in-situ plating.

It has been observed that the traditional form of bidirectional CCD testing carries with it several significant complications; for example, stripping of lithium metal may induce pore formation from the stripped side, leading to local current focusing upon plating that may invalidate the reported critical current density that the test is intended to demonstrate.[12][23][24] The propensity for void formation rises at higher current densities,[22][25] and therefore obtaining an accurate measure of CCD becomes increasingly difficult throughout the test. The inability to disentangle the overlapping failure mechanisms of dendrite nucleation and pore formation in a Li-Li cell with significant interfacial contact loss poses a challenge: to obtain a valid CCD measurement of the SE, the Li|SE interface quality and morphology must be strictly controlled throughout the measurement.[23] Such theoretical shortcomings cannot be assumed to be benign: Li-Li symmetric tests yield substantially different results for the same materials systems, [23][26][27] indicating a need for improved methods to test critical current density.

Guidelines for designing the testing protocol to determine the CCD on a given system can be derived from previous reports. A unidirectional CCD testing approach should be considered as an alternative to Li-Li symmetric cycling test to limit the overlap of different SE failure modes.[23] Avoiding the interplay between stripping and plating mechanisms at a single interface helps to better isolate the critical current density of the SE itself. Mitigation of void formation has been reported, for example, by carefully tuning the CCD test recipe parameters: maintaining small areal capacities[28] for each current step and incorporating waiting time [23] between pulses.

A final strategy reported in the literature is to incorporate pressure into the testing setup to ensure that proper contact is maintained at the Li|SE interface. [29]

We present here a high-throughput technique for unidirectional CCD testing of solid electrolyte systems. The technique presented here does not use Li foil; instead, one Li electrode (counter electrode) is evaporated onto the surface of the SE and the other lithium electrode (working electrode) is plated in-situ during an initial formation step. The test is designed to generate reliable experimental feedback in a relatively short period of time at a reasonable cost, enabling iterative materials development to improve CCD performance of SE materials much faster than alternative methods would permit. Building off previous literature, we demonstrate the importance of design parameters such as areal capacity in the CCD measurement and outline a novel framework using survival analysis for statistical comparisons of different SE populations.

The tests conducted for this work were carried out on solid separators that did not meet specifications for production quality, and therefore the results shown here should not be taken to be representative of the state of the art with regards to the separator material or production quality. Rather, this work is intended to illustrate the high-throughput CCD testing technique and give insight into analysis of the data that it generates.

2. Results and Discussion

2.1. Cell Design and Testing Setup

The Li-Li format used for our CCD measurements is illustrated in Figure 1a and Figure 1b. An array of Li electrodes is evaporated across a single separator film, enabling numerous data points to be collected from one physical separator and allowing the test to control for the effects of any localized SE defectivity. Electrodes of smaller or larger areas provide different benefits: smaller electrodes provide large quantities of CCD data, whereas larger electrodes are more sensitive to larger and less frequent defects. This work will chiefly focus on data collected with 0.16 cm^2 electrodes.

For testing, the electrochemical measurement is performed using a purpose-built milli-electrode (MIE) testing apparatus (Figure 1c), consisting of two slots which fit separator films sized to produce a commercially relevant full cell, resulting in 130 electrode pads of 4 × 4 mm each. An array of pogo pins is deployed so that each pin individually contacts the center of each electrode. The area of the testing slot and milli-electrodes can be flexibly designed to fit the desired electrode pattern and separator area. In this configuration, an individual separator can yield 130 independent CCD measurements, allowing statistically significant conclusions to be drawn about both the CCD distribution and the areal defect density.

No pressure is applied to the samples during testing, aside from the small force exerted by the pogo pin in a localized area. The lack of applied pressure necessitates a high-quality Li electrode and a pristine Li|SE interface to minimize pore formation during Li stripping. Eliminating the need for pressure offers a distinct advantage, simplifying the design of the high-

throughput testing apparatus shown in Figure 1c. It is worth mentioning, however, that applying pressure would not compromise the CCD result and could be utilized to ensure consistent interfacial contact throughout the test.[23]

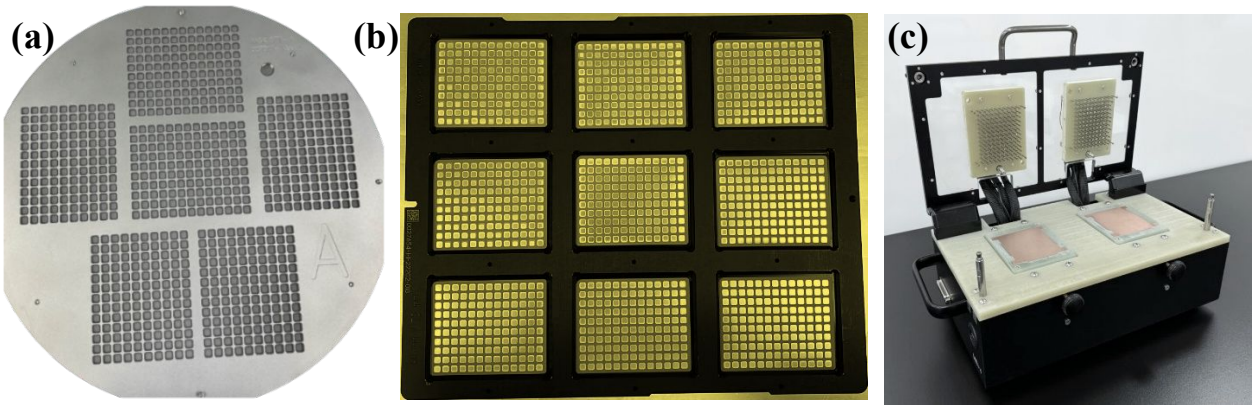

Figure 1. (a) An evaporation mask for 10 × 13 grids of 4 mm × 4 mm squares (b) False-color image of a tray of 9 ceramic films (60 mm x 75 mm) with 130 electrodes of deposited Li per film. (c) Tester designed for high-throughput CCD measurements of ceramic SE films.

The premise of the unidirectional CCD test is relatively straightforward: the SE is subjected to a galvanostatic pulse at a low current density that is increased stepwise until a sudden drop in voltage is observed, indicative of a short circuit due to Li dendrite penetration across the SE. The current density at which the short is observed is recorded as the CCD. Current passes in one direction for a unidirectional test, and therefore the sign of the voltage does not change throughout the test. An example of a typical voltage and area-specific resistance (ASR) response is provided in Figure 2a and Figure 2b. The ASR of an electrochemical device can be calculated from Ohm's Law using the working voltage, V, the resting voltage, V_0, and the current density, i:

$$ASR = \frac{V - V_0}{i} \quad (1)$$

For symmetric Li-Li cells, the resting voltage, V_0, is 0 V, making it straightforward to calculate continuous ASR values throughout the CCD measurement, in contrast to full cells where the cell must rest to get an accurate measurement of V_0 at any point in the cycle. Reporting the raw data from the CCD test as ASR versus areal capacity helps to highlight any impedance rise that occurs prior to a short.

One of the main advantages of the unidirectional CCD test is the ability to decouple the plating and stripping interfaces, enabling straightforward diagnosis of cell failure mechanisms based on the voltage response. For example, impedance growth is a signature of contact loss due to pore formation in the Li at the stripping interface, leading to non-uniform current flux across the area of the electrode. Once the surface area of a pore exceeds the thickness of the solid electrolyte, the Li flux at the plating interface will exhibit nonuniformities.[30][31] Thin electrolytes, such as the SE characterized in this study (in the range of 20–40 μm), will be especially prone to current focusing at the plating interface given small amounts of contact loss at the stripping interface. A valid measurement of the CCD of a solid electrolyte can only be obtained in the absence of current focusing at the plating interface; tests with impedance growth prior to the short are thus considered compromised tests (Figure 2c and Figure 2d). In survival analysis these tests are censored[32] from the pulse where ASR exceeds a 10% increase from the initial ASR, and subsequent pulses are removed from the population regardless of whether a short is observed or not. The threshold for censoring is the minimum increase which could be reliably detected without introducing meaningful risk of false positives; this threshold was determined to be 10% in the case of the specific electrolyte material, geometry, and test

equipment used. A sensitivity analysis was used to confirm that censor thresholds between 5% and 40% ASR growth do not invalidate the survival data or conclusions presented in this work.

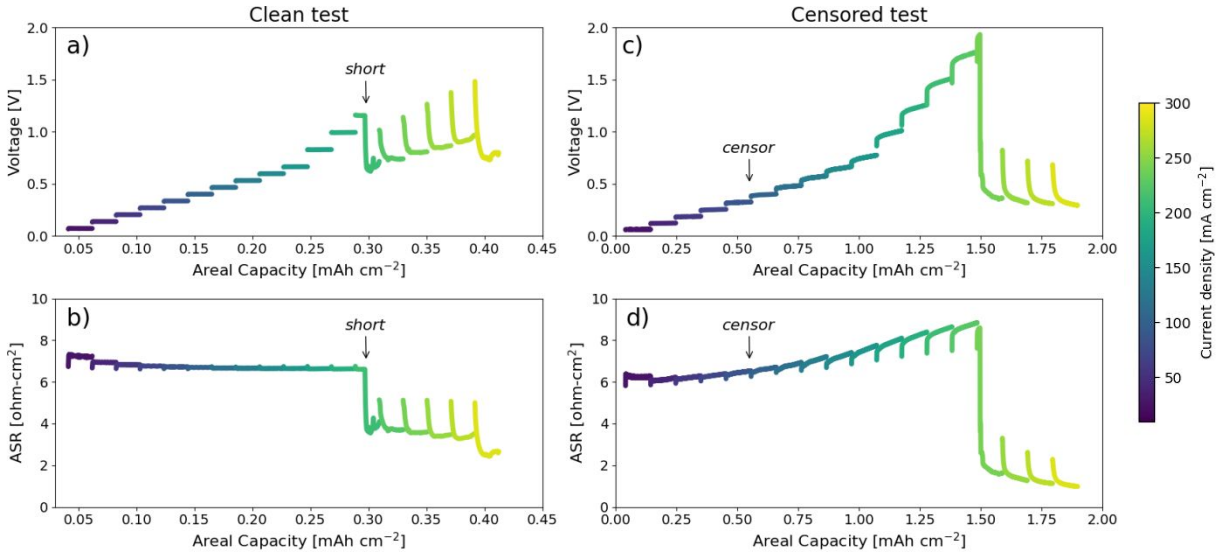

Figure 2. (a) Voltage response and (b) area-specific resistance response from a CCD measurement of a single 0.16 cm^2 Li electrode at T=25^{0}C. (c, d) Result exemplifying a compromised test, where impedance growth manifests as an increase in voltage and ASR prior to the short.

2.2. Validation of the Capacity-Controlled CCD Test

The probability of pore formation at the interface of the stripped Li anode has been shown to increase with both current density and capacity (or time, as capacity corresponds to time in a test with constant current).[33]–[36] Therefore, to design a CCD test that reaches high current densities, it is advantageous to use shorter pulses to minimize the quantity of data that must be censored due to impedance growth. The length of each pulse can be defined using one of two methods: 1) time-controlled pulses, where the step capacity increases gradually throughout the test[22] or 2) capacity-controlled pulses, where the step time decreases gradually throughout

the test.[20][37] Table 1 highlights the differences in cumulative test time and Li thickness required to run a capacity- or time-controlled test with different pulse lengths. For the time-controlled approach, step times of 10 min[38], 30 min[39][40], or 1 hour[41] are common. Such a long pulse length is impractical for a test of current densities as high as 300 mA cm^{-2}, as Li thickness would need to be on the order of millimeters.

As opposed to using a time-controlled test, using capacity-controlled pulses provides valid data while minimizing the total test time and amount of Li required to complete the measurement. This capacity-controlled limit is important because, while the use of evaporated Li as a reservoir is preferable to manage confounding factors such as SE interface quality, it is relatively more costly and operationally complex compared to using Li-metal foil. Using capacity-controlled pulses of 0.1 μm is also relatively fast, enabling over 1200 CCD measurements per day from a single testing apparatus.

Table 1. Cumulative Li thickness and time required for capacity-controlled and time-controlled tests with different pulse lengths.

Test type	Pulse length	Total Li (μm)	Total time (min)	Tests per day*
Capacity controlled	0.1 μm	1.8	1.9	1204
	0.3 μm	5.4	2.7	841
	0.5 μm	9.0	3.6	646
Time controlled	10 sec	30.3	4.5	512
	30 sec	90.9	10.5	219
	50 sec	151.6	16.5	139

**assuming 80% uptime using a two-slot tester (Figure 1c) over a 24-hour period*

Simplified calculations can give a rough estimation of the areal capacity required for a dendrite to penetrate the separator under investigation. The premise of the CCD measurement is to observe the instance of a dendrite at the critical current density; therefore, the total charge passed during each pulse must exceed the charge required to form a dendrite large enough to

detect a drop in the voltage response. Table 2 gives an estimation of the capacity required for a dendrite with cylindrical geometry to penetrate the separator using dendrite height of both 20 µm and 40 µm, as the separators in this study have a thickness in this range. The areal capacity for a 0.16 cm^2 electrode is added to Table 2 to give a direct comparison against pulse length reported in this study, which is primarily 0.021 mAh cm^{-2}. For dendrite diameters up to 200 µm, areal capacities remain below 0.021 mAh cm^{-2}, suggesting that a 0.1 µm pulse length is sufficient to characterize the CCD of the thin ceramic electrolytes used here, a conclusion which is empirically validated later in this section. For many academic settings, separators may be at least 10x the thicknesses of the separators characterized in this work and hence require 10x the areal capacity for a dendrite to penetrate the separator, depending on the electrode size used for the measurements. For these systems, a pulse length of 0.1 µm may not be sufficient.

Table 2. Capacity required to capture a single Li dendrite assuming the dendrite forms a cylinder the thickness of the ceramic separator. Areal capacity is calculated for a 0.16 cm^2 electrode, assuming all lithium inventory available across the electrode area is focused on the dendrite. Estimates are provided for 20 µm and 40 µm separator thickness at four different dendrite diameters: 5, 50, 100, and 200 µm.

Dendrite height (µm)	*Dendrite diameter (µm)*	*Dendrite volume (cm^3)*	*Capacity to dendrite (mAh)*	*Areal capacity to dendrite (mAh cm^{-2})*
20	5	3.93×10^{-10}	8.10×10^{-7}	0.00001
20	50	3.93×10^{-8}	8.10×10^{-5}	0.00051
20	100	1.57×10^{-7}	3.24×10^{-4}	0.00202
20	200	6.28×10^{-7}	1.30×10^{-3}	0.00810
40	5	7.85×10^{-10}	1.62×10^{-6}	0.00001
40	50	7.85×10^{-8}	1.62×10^{-4}	0.00101
40	100	3.14×10^{-7}	6.48×10^{-4}	0.00405
40	200	1.26×10^{-6}	2.59×10^{-3}	0.01619

To further validate 0.1 µm capacity-controlled testing, we investigate the distribution of short behavior across a large volume (N=370) of CCD measurements tested with fixed pulse-

lengths of 0.1, 0.3, and 0.5 μm of Li, equivalent to areal capacities of 0.021, 0.063, and 0.105 mAh cm^{-2}. We define the parameter Q_{short}, the capacity-to-dendrite of the shorted pulse. Note that Q_{short} is not cumulative from the beginning of the test but rather is measured from the beginning of the pulse. This metric captures how much charge is passed at the critical current density prior to the sharp voltage drop indicative of short circuit. Figure 3 shows the distribution of Q_{short} obtained from CCD tests where a short was observed; censored tests are not included in this analysis. Failures tend to be clustered within the first 0.1 μm of plated Li, with a median in the narrow range of 0.039 to 0.046 μm (0.008 to 0.0095 mAh cm^{-2}) for all pulse lengths. The distribution of Q_{short} gives a measure of the total capacity required for a dendrite to nucleate, propagate the length of the separator, and grow large enough to be detectable in the voltage signal. For the tests using pulse-lengths of 0.3 and 0.5 μm of Li, roughly 75% of the shorts were observed in the first 0.1 μm of the pulse. This suggests that, for the SE used in this study, capacity-controlled measurements using pulse-lengths of 0.1 μm will capture 75% of the shorts at the true critical current density (the current density that would be observed using longer pulses); the remaining 25% of shorts are assumed to occur in the subsequent pulse at the next-highest current density.

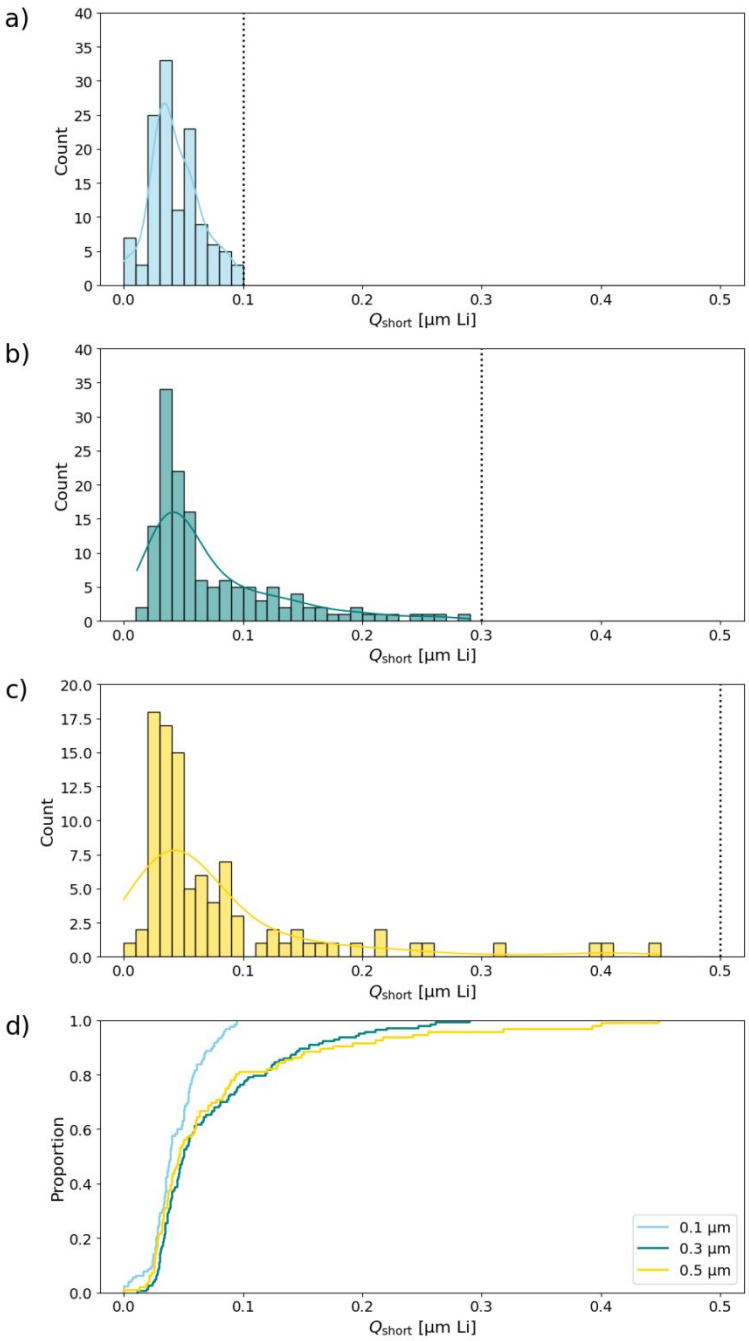

Figure 3. Distribution of Q_{short} for three different test recipes: a) 0.1 µm pulses, b) 0.3 µm pulses, and c) 0.5 µm pulses. The dotted line shows the end of the pulse. d) Cumulative distribution function (CDF) plot for Q_{short}. Proportion of Q_{short} observed by 0.1 µm is 100% (128/128) for 0.1 µm pulses, 76% (110/144) for 0.3 µm pulses, and 80% (78/98) for 0.5 µm pulses.

A population-level comparison of CCD results using 0.1, 0.3, and 0.5 µm pulses can be achieved using survival analysis, as seen in Figure 4. With this approach, the survival probability

is reported as a function of current density using a Kaplan-Meier survival curve, capturing both shorted and censored data points at each current density. Additional details including the Python packages used for this survival analysis are included in the SI. Electrode pads that survive the duration of the test without shorting are censored at the maximum current density of 300 mA cm^{-2}. The survival curves shown in Figure 4 suggest that 0.1 µm provides sufficient capacity per pulse to observe a short at each current density step: measurements of CCD using 0.1 µm, 0.3 µm, and 0.5 µm pulse lengths are statistically indistinguishable.

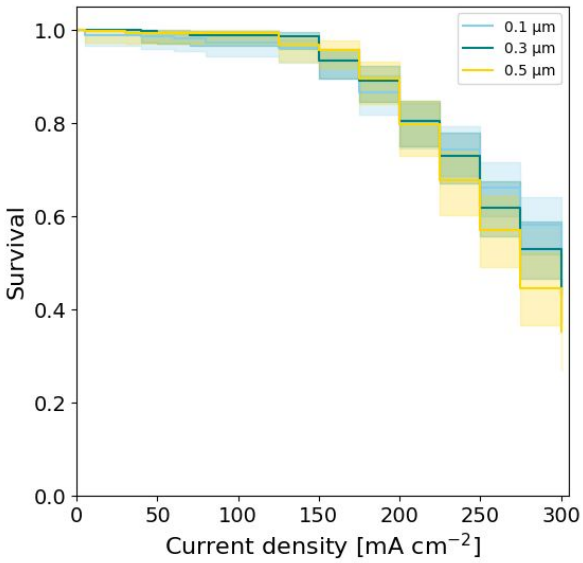

Figure 4. Survival distribution from CCD measurements using different lengths for each charge step. Electrode pad area is 0.16 cm^2 and T = 25 ^{0}C. Solid line represents survival estimate for each current density and shaded regions are the 95% confidence intervals. Python packages used for this analysis are detailed in the SI.

Statistical comparison of CCD populations can be performed using traditional statistical methods such as restricted mean survival time (RMST) analysis.[42] When comparing different populations at a specified current density, RMST computes the population average survival time up to the current density of interest by calculating the area under the Kaplan-Meier survival curve. RMST analysis provides a more rigorous means for comparison between two populations

than comparing survival proportions alone, as RMST analysis accounts for censoring, is non-parametric (does not assume a functional form for the survival function) and allows confidence intervals for survival to be calculated. For this analysis, three different current densities are selected as points of comparison: 100 mA cm^{-2}, 200 mA cm^{-2}, and 299.999 mA cm^{-2}. At each current density, the difference in means of the restricted mean survival time, Δ RMST, between 0.1 µm, 0.3 µm, and 0.5 µm pulse lengths is calculated to determine if the results shown in Figure 4 are statistically differentiated. Table 3 shows that, for all points of comparison, the p–value is larger than 0.05 and the confidence intervals contain zero. This demonstrates that pulse lengths between 0.1 µm and 0.5 µm do not produce significantly different survival data in a study with 80% statistical power to detect a survival difference of 6%, 11%, and 13% at the current densities of 100 mA cm^{-2}, 200 mA cm^{-2}, and 299.999 mA cm^{-2}, respectively.

Table 3. Comparison of the difference in means of the RMST for the survival data reported in Figure 4. The RMST p-values were calculated using the lifelines package in Python. A value of $\alpha = 0.05$ is assumed for all comparisons.

Current density (mA cm^{-2})	*Comparison*	*p–value*	*Δ RMST (mA cm^{-2})*	*Δ RMST $LCI - UCI$ (mA cm^{-2})*
100	0.1 µm < 0.3 µm	0.15	1.13	-0.40 – 2.66
	0.1 µm < 0.5 µm	0.23	1.03	-0.64 – 2.69
	0.3 µm > 0.5 µm	0.85	-0.11	-1.22 – 1.01
200	0.1 µm < 0.3 µm	0.22	2.74	-1.62 – 7.09
	0.1 µm < 0.5 µm	0.20	2.99	-1.54 – 7.52
	0.3 µm < 0.5 µm	0.89	0.26	-3.44 – 3.95
299.9	0.1 µm < 0.3 µm	0.98	0.11	-9.79 – 10.00
	0.1 µm > 0.5 µm	0.42	-4.40	-15.04 – 6.25
	0.3 µm > 0.5 µm	0.38	-4.50	-14.48 – 5.48

Despite producing equivalent survival results to 0.1 and 0.3 µm recipes, tests with 0.5 µm pulse length had higher incidence of impedance growth, resulting in more datapoints potentially compromised by the confounding effects of stripping porosity and therefore censored from the

population. The consequence of choosing a test condition with excessively long pulses is a large fraction of data which must be censored mid-test, resulting in larger confidence intervals in the survival analysis and limiting the ability to make statistically significant conclusions for a given sample size.

Approximately 35% of the pads in Figure 4 showed no indication of a short up to 300 mA cm^{-2} for areal capacities up to 0.105 mAh cm^{-2} (0.5 μm pulse length). To confirm the validity of this CCD performance when applied over much higher capacities, we performed a separate set of measurements in which electrode pads were first subjected to the CCD test described here, but the test was followed by an additional 50 pulses of plating at 300 mA cm^{-2}, equivalent to 5 μm Li (1.05 mAh cm^{-2} of capacity). Of those electrode pads that survived the initial CCD test, 87% sustained the additional 50 pulses at 300 mA cm^{-2} without shorting (Figure SI-1). Thus, survival obtained using the fixed-capacity test with a pulse length of 0.1 μm is a good approximation, within 80%, of the proportion of cells that can sustain capacities above 1 mAh cm^{-2} at a given current density.

To balance requirements for data quality, total test capacity, and complexity of sample preparation, 0.1 μm pulse length is used for the following data presented in this work.

2.3. Scaling for Differences in Temperature or Area

While most reports of CCD in literature provide single values of current density, reporting CCD as a survival curve offers several advantages. The probability of survival can be extracted with confidence intervals at any current density. In addition, survival curves can be transformed as a function of electrode size or temperature.

To capture the impact of temperature on dendrite-resistance of the solid electrolyte, CCD measurements were performed on 0.16 cm^2 millielectrodes (MIE1) at T = 15 ^{0}C, 25 ^{0}C, 30 ^{0}C, and 45 ^{0}C and 2.75 cm^2 millielectrodes (MIE3) at T = 15 ^{0}C, 25 ^{0}C, and 30 ^{0}C. Kaplan-Meier survival curves for each condition are provided in Figure 5a and Figure 5b. CCD increases with increasing temperature in both small and large electrode sizes, which may be attributed to the increased softness of Li metal at elevated temperatures, as suggested by previous reports. [22][43]–[46] Weibull parameteric modeling is a common tool used in survival analysis to model the time-to-failure across a wide array of applications.[47] We use Weibull fitting to capture the temperature-dependence of survival data in Figure 5a and Figure 5d.

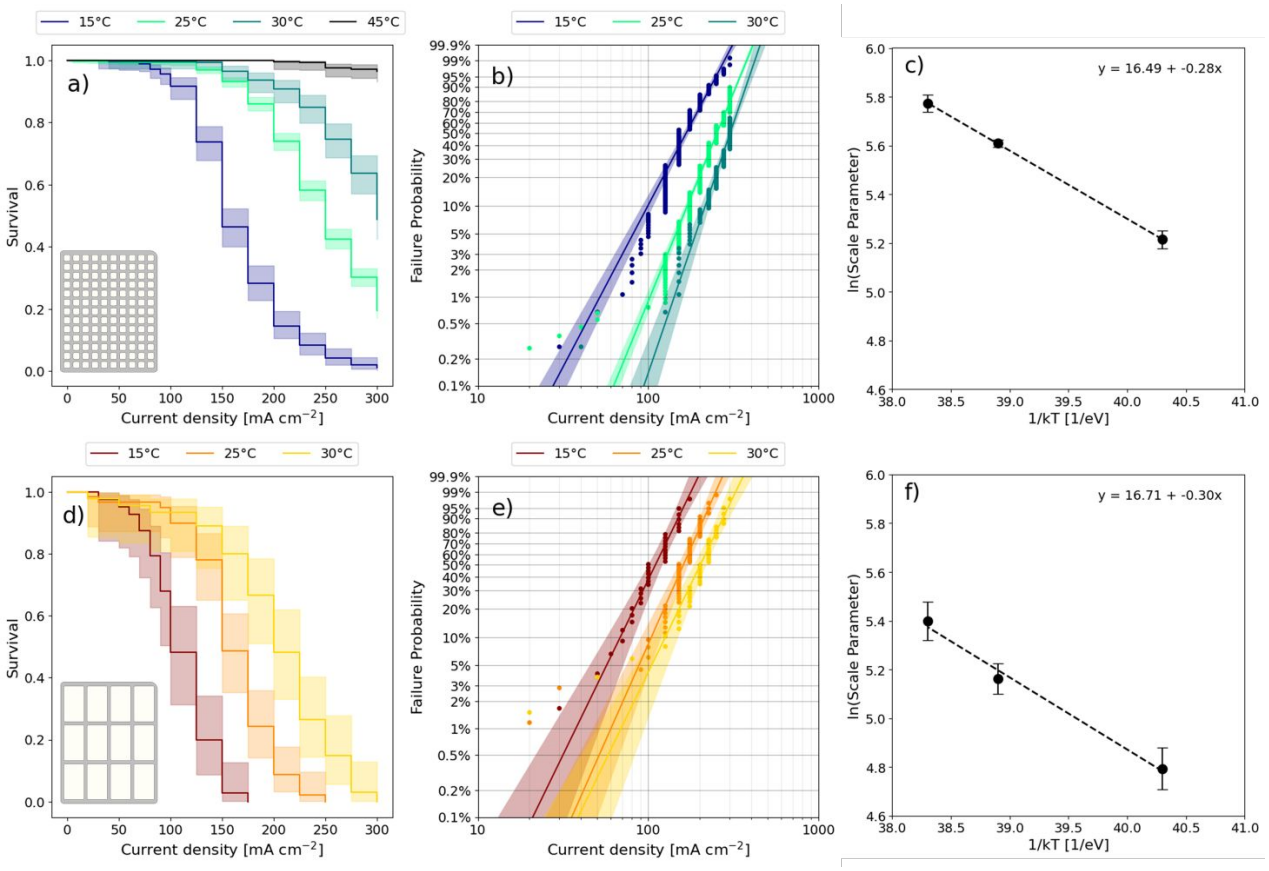

Figure 5. a) CCD survival distribution using 0.16 cm^2 electrodes tested at 15 ^{0}C (N = 254), 25 ^{0}C (N= 1018), 30 ^{0}C (N= 253), and 45 ^{0}C (N= 256). Solid line represents survival estimate for each current density and shaded regions are the 95% confidence intervals. The inset shows a

schematic of 130 electrodes with area = 0.16 cm^2 deposited across a 60 × 75 mm separator. b) The 0.16 cm^2 electrode survival data on a Weibull probability CDF plot. Lines show the fits to the Weibull distribution for each temperature and shaded regions are the 95% confidence intervals. c) Weibull scale parameter on an Arrhenius plot with the equation for the best fit line included in the figure. d) CCD survival distribution using 2.75 cm^2 electrodes tested at 15 ^{0}C (N = 43), 25 ^{0}C (N= 60), and 30 ^{0}C (N= 46). The inset shows 12 electrodes with area = 2.75 cm^2 deposited across a 60 × 75 mm separator. e) & f) Same figures as b & c for CCD measurements using 2.75 cm^2 electrodes. Python packages for generating survival and Weibull plots are provided in the SI.

The strength of ceramic materials can be described by a Weibull distribution, which is explained by the "weakest link theory," where failure is governed by the largest flaw in the material.[48] Similarly, the failure of ceramic solid electrolytes is often attributed to localized microstructural defects or flaws.[49] In this context, the applied plating current density in symmetrical Li cells is analogous to applied stress in a mechanical strength test. Dendrite formation and propagation are considered to be mechanical phenomena caused by current focusing and presence of flaws such as microcracks and subsurface voids.[49][50] Consequently, the critical current density is determined by the most extreme flaw present in the tested milli-electrodes. The cumulative failure probability, P_f, is expressed by:

$$P_f = 1 - \exp\left[-\left(\frac{i_c}{i_{c0}}\right)^k\right] \quad (2)$$

where i_c is the current density at failure, i_{c0} is the Weibull scale parameter (the characteristic current density corresponding to the 63rd percentile of failure), and k is the Weibull shape parameter or modulus. The characteristic current density serves as a scale parameter, where a higher value shifts the distribution towards higher CCDs. The Weibull modulus represents the inverse of the flaw distribution width; a larger modulus indicates a narrower distribution of flaws, implying more uniformity in the material's flaw population.

Both extrinsic and intrinsic flaws can contribute to dendrite formation, thereby impacting the critical current density (CCD). Extrinsic flaws are typically macroscopic defects, such as those arising from fabrication processes, while intrinsic flaws include microstructural imperfections such as microcracks, voids, chemical inhomogeneities, and grain boundaries. The distinction between these two types of flaws is important because they originate from different flaw distributions, each characterized by distinct Weibull shape and scale parameters. Understanding these differences enables more targeted approaches to improving material performance and reliability.

Figure 5b and Figure 5e show the temperature- and area-dependent CCD measurements from Figure 5a and Figure 5d plotted in Weibull scale. The line drawn through each dataset shows the Weibull distribution (Equation 2) that best fits the dataset (maximum likelihood estimation). Table 4 gives the resulting shape parameter k and the scale parameter i_{c0} obtained from these fits, as well as the lower and upper confidence intervals (95%) for each. The value of i_{c0} shows a strong dependence on temperature, T, shifting to higher values as the Li becomes softer with temperature, thereby reducing the probability of failure at a given current density. As expected, the shape parameter k does not show any significant temperature dependence since the flaw distribution is independent of test T. Note that Weibull fit data for the 0.16 cm^2 electrodes measured at 45^{0}C is not reported here, as >90% of the tested electrodes never shorted, and therefore the predicted shape and scale parameters had very large confidence intervals.

The temperature dependence of i_{c0} for both electrode sizes follows an Arrhenius dependence,[22][43]–[45] as shown by the linear fit in Figure 5e and Figure 5f. The slope of the best-fit line on the Arrhenius plot gives the activation energy, E_A, which was 0.28 eV and 0.30 eV for the 0.16 cm^2 and the 2.75 cm^2 electrode data respectively. The similar slope values demonstrate

that CCD survival data follows the same temperature dependence regardless of the size of the electrodes used for the measurement. The value of E_A can be used to calculate the characteristic current density i_{c0} at any temperature using the following equation:

$$\frac{i_{c01}}{i_{c02}} = \exp\left[\frac{E_A}{k_B}\left(\frac{1}{T_1} - \frac{1}{T_2}\right)\right] \quad (3)$$

Using Equation 2, it is straightforward to derive an equation for converting probability of survival measured from one set of test conditions, P_{s1}, to probability of survival for a different set of test conditions, P_{s2}, assuming the scale parameters, $i_{c01}$and i_{c02}, for each condition are known:

$$\ln[P_{s2}] = \ln[P_{s1}]\left(\frac{i_{c01}}{i_{c02}}\right)^k \quad (4)$$

Here, we assume the shape parameter, k, is independent of test conditions such as temperature, as demonstrated by the fit parameters in Table 4.

Combining Equation 3 and Equation 4, we obtain a final equation for translating survival data to new temperatures:

$$\ln[P_{s2}] = \ln[P_{s1}]\left(\exp\left[\frac{E_A}{k_B}\left(\frac{1}{T_1} - \frac{1}{T_2}\right)\right]\right)^k \quad (5)$$

Table 4. Weibull fit parameters from CCD survival data shown in Figure 5.

Area [cm^2]	T [^{o}C]	$1/k_BT$ [1/eV]	k	$k\ (LCI - UCI)$	i_{c0} [mA cm^{-2}]	$i_{c0}(LCI - UCI)$
0.16	15	40.3	3.65	3.34 – 4.02	183.9	177.3 – 190.7
0.16	25	38.9	4.70	4.43 – 4.99	272.9	268.8 – 277.0
0.16	30	38.3	5.63	4.84 – 6.72	321.5	310.6 – 332.9
2.75	15	40.3	3.95	3.16 – 5.27	120.7	110.8 – 131.5
2.75	25	38.9	4.34	3.59 – 5.47	174.5	164.1 – 185.7
2.75	30	38.3	3.96	3.16 – 5.32	221.2	204.5 – 239.3

The activation energy found in these measurements, 0.28–0.30 eV, is likely dictated by several underlying phenomena, including lithium diffusivity in the solid electrolyte[43][44], electrolyte-electrode interfacial resistance[44], lithium self-diffusivity[51], and lithium creep[46]. A careful study over a wider temperature range using different solid-electrolyte and electrode materials would be necessary to deconvolute the contributing factors.

Larger electrodes have a higher probability of containing more severe defects, leading to a greater likelihood of failure (lower CCD).[48] Comparing the survival data for 0.16 cm^2 electrodes in Figure 5a with the 2.75 cm^2 electrodes in Figure 5b, it is clear that smaller electrodes result in higher CCD values across all temperatures. Thus, it is critically important to clarify the electrode size when reporting CCD measurements. The value of i_{c0} for any area, A_2, can be calculated if i_{c0} and k are known for a single area, A_1, using the following relationship:[48]

$$\frac{i_{c01}}{i_{c02}} = \left(\frac{A_2}{A_1}\right)^{\frac{1}{k}} \tag{6}$$

Substituting Equation 6 into Equation 4, we obtain a final equation that can be used to scale survival data from electrode 1 to survival of electrode 2 using the area ratio, A_2/A_1, of the two electrodes:$P_{s2} = P_{s1}^{\frac{A_2}{A_1}}$ (7)

When comparing the CCD of compositionally different solid electrolyte materials, it is important to correct for temperature and electrode size before drawing conclusions. Equation 5 and Equation 7 introduce a framework for scaling survival data to correct for difference in temperature or area. To demonstrate the efficacy of this framework, we take the CCD survival data in Figure 5 and scale it to $T = 25^0$C and area = 1 cm^2. The resulting survival curves collapse together, as shown in Figure 6. After scaling data to a unified temperature using Equation 5,

CCD survival from 15^0C, 25^0C, and 30^0C becomes indistinguishable (underlying data presented in Figure SI-3), supporting the claim that CCD survival can be translated to a different temperature if the Arrhenius behavior is known. Figure 6 also demonstrates the efficacy of the area-scaling model, where CCD survival data using 0.16 and 2.75 cm^2 electrodes is scaled to a unified electrode area using Equation 7. The shapes of the scaled survival curves are closely matched, though there is a small offset and the data from the 0.16 cm^2 electrodes falls slightly below that the 2.75 cm^2 electrodes for all three temperatures. (Figure SI-4). This is in contrast with to the unscaled CCD measurements in Figure 5, where the survival of the 0.16 cm^2 electrodes is higher than that of the 2.75 cm^2 electrodes measured using the same test conditions. The offset of scaled survival data from small and large electrodes suggests one potential limitation in the model described by Equation 7; while the model assumes that the current distribution is even across the electrode, a non-negligible amount of current focusing may occur near the edge of the Li electrodes, and such edge effects may be the reason that the scaled survival of the small electrodes is slightly lower than would be expected. More work remains to define the underlying mechanisms that govern the area dependence of CCD.

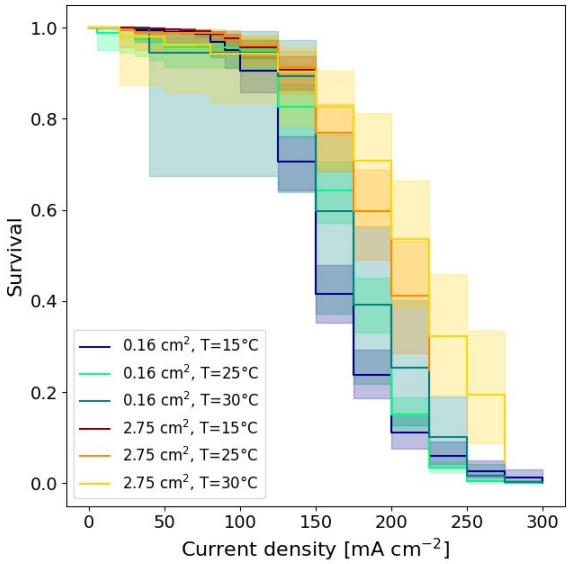

Figure 6. Scaled CCD survival data from 0.16 cm^2 electrodes and 2.75 cm^2 electrodes measured at different temperatures. Using Equation 5 and Equation 7, original survival data and confidence intervals are scaled to a single temperature ($T = 25^0$C) and area (1 cm^2), enabling direct comparison between the measurement results from different test conditions. Original data, shown in Figure 5a and Figure 5d, was collected on the same solid electrolyte.

2.4. Testing Throughput and Development Progress

This testing methodology enables high-throughput testing of SE materials, allowing the generation of very high-N datasets within a practical timeframe and at a reasonable cost. This allows researchers to draw statistically significant conclusions about materials properties and behavior, iterate on materials development more rapidly, and to develop materials with improved CCD and lower defectivity. As a result of the condensed test recipe, large amounts of data can be generated in relatively short periods of time: Figure 7 shows the cumulative pad-level data generated by a single MIE tester over the course of several years; such a device supports extremely high-throughput data generation, and these volumes still do not reach the maximum throughput of the testing apparatus.

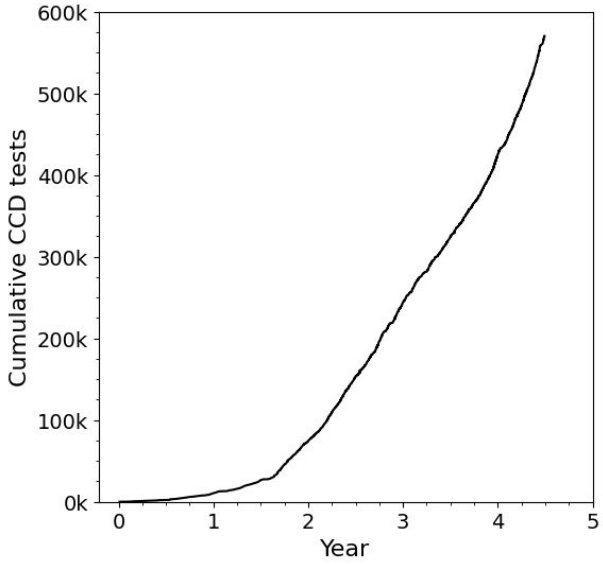

Figure 7. Cumulative individual pad-level CCD measurements generated by a single two-slot MIE testing apparatus over the course of a ~4 year period.

This high-throughput technique has allowed rapid iteration of materials and process development, resulting in substantial improvements to CCD performance of a ceramic SE material. As Figure 8 shows, over several successive generations of materials development, CCD_{max} of the material system was increased from ~60 mA cm^{-2} to at least 300 mA cm^{-2} (the maximum measurable CCD of the test protocol as described here), and average CCD_{min} and areal defect density also saw improvement. The development result reported here is a CCD_{max} of 300 mA cm^{-2} with over 90% survival of electrode pads. Commercial applications, such as electric vehicles, typically require significantly lower critical current density thresholds but also separator parts with areas several orders of magnitude larger than an individual electrode pad; the scaling estimator presented in Equation 7 allows a survival projection for separators of arbitrary area across a range of current densities, allowing rough order of magnitude estimation of robustness across applications.

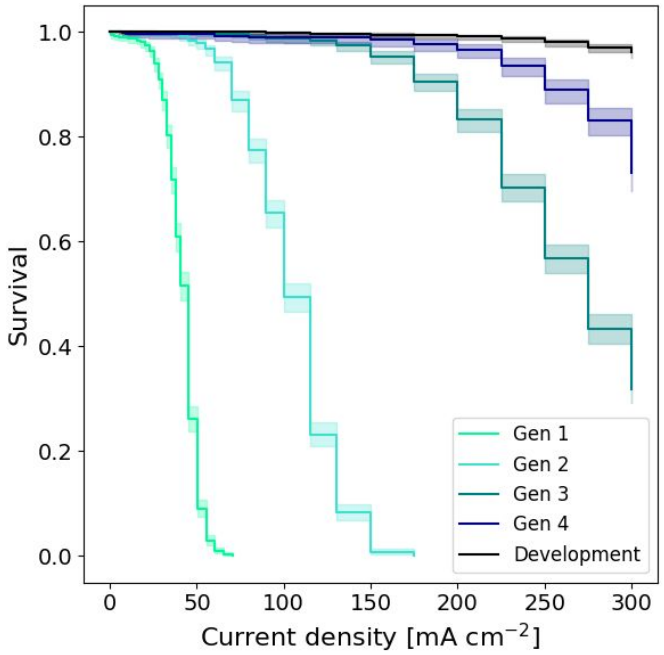

Figure 8. Evolution in CCD performance with successive generations of a ceramic solid electrolyte material. Solid line represents survival estimate for each current density and shaded regions are the 95% confidence intervals. The dataset for each generation is an aggregate of separators from several batches per generation. The sample size of electrode pads per generation is: Gen 1 (N = 1292), Gen 2 (N= 1280), Gen 3 (N= 1338), Gen 4 (N= 790), and Development (N=1675). "Development" refers to an iteration of the ceramic separator material under development. Electrode pad area is 0.16 cm^2 and T = 30 ^{0}C.

3. Conclusion

One of the most significant hurdles to developing better solid electrolyte materials is a lack of reliable, large-N datasets on materials properties, including CCD. Without a testing methodology that limits confounding effects and permits high-throughput data collection, rapid and systematic materials development is much more difficult. The experimental method presented here enables the collection of large datasets and permits reliable inference about materials properties, including CCD and defect density. The technique described here has been one important contributor to the development and demonstration of SE materials with CCD and areal defect density of the order necessary to enable the commercial use of SE materials in automotive applications.[52]–[54]

The results of this high-throughput testing and materials development suggest several best practices for CCD testing and reporting. CCD testing methodology should take care to isolate the effects of Li stripping porosity from the measurement of SE CCD, for example by performing unidirectional tests and validating the use of shorter capacity-controlled pulse steps. Any measurement of CCD performance is also strongly dependent on electrode area, due in part to the impact of areal density of localized defects, and results of CCD testing should be reported and analyzed in light of this. Lastly, the use of survival plots and Weibull analysis, rather than single values for CCD, allows researchers to better understand the behavior of the material system in question and draw statistically significant conclusions about experimental interventions. Widespread adoption of these best practices would help accelerate advances in the field and speed the development of commercially relevant SE materials.

4. Experimental Section

Ceramic SE separators with thicknesses in the range of 20–40 μm are used in a symmetric configuration (Li|SE|Li) to evaluate CCD. Separators selected for this work were deficient with respect to one or more production quality specifications so as to avoid impacting commercial operations. For the purposes of this particular test, evaporation physical vapor deposition (PVD) is used to deposit thin Li counter electrodes on the stripping side of the SE. Ceramic separators are inserted in the designated slots within a metallic mask. Different mask designs may be used to accommodate a variety of separator and electrode sizes. Figure 1a shows a mask that can hold six 60 × 75 mm separators with a 10 × 13 array of 4 × 4 mm openings. The masks are loaded into the evaporator with exposed side facing down.

The Li evaporation PVD process is started once the vacuum chamber reaches a vacuum level of 10^{-8} Torr. Deposition takes places in two steps. The process begins with a pre-deposition step where a Li-containing stainless-steel crucible is heated until a steady rate of deposition is reached. During this step, the crucible is fully covered by a shutter, such that no Li would deposit onto the SE. After a desired evaporation rate of ~50-60 Å s^{-1} is reached, the shutter is opened, and lithium deposition begins. After the target Li thickness is achieved, the shutter is closed, power to the crucible is turned off, and the chamber begins to cool down. Once the chamber reaches room temperature and pressure, deposited films are unloaded from the masks and transferred to test trays. The entire process takes place in a dry room where the temperature is 19.4 ℃ ± 1.1 ℃ and the dewpoint temperature is -45 ℃ to -60 ℃. Sample extraction from the PVD equipment is safe to perform since the atmosphere is non-reactive to the ceramic separators with thin Li counter electrodes.

Figure 1b shows a false-color image of a tray holding nine SE separators with 0.16 cm^2 electrode pads deposited across the surface. A custom-built electrical tester is used to measure CCD: Figure 1c demonstrates a two-slot tester that is used to measure the critical current density of individual 0.16 cm^2 milli-electrodes shown in Figure 1b. Gold-coated flat-head low-spring test probes (Test Connections Inc) are used for electric contact between tester and the deposited Li. The spring force on the pin was calculated to be 0.2 N and contacts 1.77 mm^2, or 11% of the deposited Li area. No additional external pressure is applied during the test. The test is performed sequentially on the milli-electrodes so the potentiostat records only one electrical result at a time, which enables the use of one current collector in the electrical configuration. The current collector forms a planar interface with the SE across the full separator area (60 x 75 mm) and is applied in the same fashion as it would be in the full-cell configuration. The current collector side of the sample is positioned directly against a copper plate, ensuring direct contact with the tester. Figure 9 provides a schematic representation of the various components in the symmetric configuration. The figure is not drawn to scale, but accurate dimensions are included where necessary.

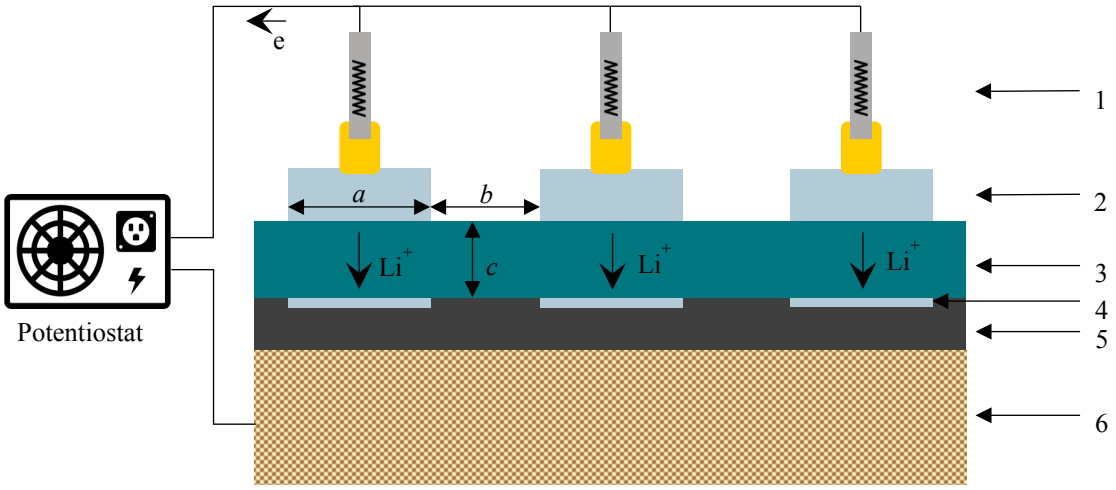

NOT TO SCALE (a = 4 mm, b = 1.5 mm, c = ~20–40 μm)

1. Pogo pins (spring force= 0.2 N)
2. Stripping electrode (CE, vapor-deposited Li)
3. Solid electrolyte
4. Plating electrode (WE)
5. Current collector
6. Copper base

Figure 9. A schematic representation of the various components in the symmetric configuration.

The testing apparatus includes a series of printed circuit boards are multiplexed together to control a system of relays that direct current to the desired pogo pin. To communicate with the controller, we use an analog signal generated in the External Device Control settings of the VMP3e or VMP-300 BioLogic potentiostat in combination with the EC-Lab software. Multiple test slots are installed per electrical tester to maximize the CCD testing capacity; each testing slot has an independent relay system that is controlled by a single channel on the Biologic.

Unidirectional tests in which lithium is consistently plated at one electrode and stripped at the other electrode are used to evaluate the critical current density (CCD) of each individual milli-electrode. The plating-side Li electrode is anode-free as manufactured and is formed in-situ

by plating an areal capacity of 0.042 mAh cm^{-2}, equivalent to a lithium thickness of 0.2 μm Li, at the electrolyte-current collector interface at a rate of 5 mA cm^{-2}. The formation conditions were chosen to create a fresh and uniform SE|Li interface while balancing the need to limit formation time and required total quantity of Li. For researchers investigating systems which do not use an anode-free configuration, evaporated Li may also be used to produce the plating-side working electrode. Formation is carried out on all the individual milli-electrodes before the unidirectional test begins. Shorts observed during formation are included in the survival analysis. After all the individual working electrodes were formed, each unique pair of counter and working electrodes was tested sequentially, moving row by row from the top-left to the bottom-right.

The unidirectional CCD test recipe presented in Table 5 includes 19 steps up to 300 mA cm^{-2}. This recipe was used to generate survival shown in Figures 2 through 6, though some of the data presented in Figure 8 was gathered using finer-grained step sizes with a different number of total pulses. The initial pulse of the CCD measurement is conducted at a current density with a low probability of failure, as the goal is to observe the short instance after the formation of a Li working electrode. In this test, 5 mA cm^{-2} is the initial current density. Step size for the current density of each subsequent pulse can be calibrated as appropriate for the resolution desired to study relevant properties of the SE system under investigation. The procedure uses step sizes that grow incrementally at 10 mA cm^{-2} for steps between 10–100 mA cm^{-2} and 25 mA cm^{-2} for steps between 100–300 mA cm^{-2}. Finer step sizes may be used, though additional pulses add to the total test time and sample preparation time, as a thicker Li reservoir must be deposited to accommodate increased cumulative capacity in a unidirectional test. The areal capacity of each pulse is fixed at 0.021 mAh cm^{-2}, equivalent to a plated Li thickness, t_{Li}, of 0.1 μm as calculated using Equation 8:

$$t_{Li} = \frac{QM_{Li}}{F\rho_{Li}} \quad (8)$$

Here, Q is the areal charge capacity passed in C/cm^2, M_{Li} is the molar mass of Li (6.94 g/mol), F is Faraday's constant (96485 C/mol), and ρ_{Li} is the density of Li taken to be 0.534 g cm^{-3} for tests at 25^{0}C.

Table 5. Test recipe for unidirectional CCD. Step 1 represents the formation step. Pulse length is fixed at a capacity equivalent to 0.1 µm Li plated.

Step	I (mA cm^{-2})	pulse time (s)	rest time (s)	Cumulative areal capacity (mAh cm^{-2})	Li plated (µm)
1	5	29.7	5	0.042	0.2
2	10	7.42	5	0.063	0.1
3	20	3.71	5	0.084	0.1
4	30	2.47	5	0.105	0.1
5	40	1.86	5	0.126	0.1
6	50	1.48	5	0.147	0.1
7	60	1.24	5	0.168	0.1
8	70	1.06	5	0.189	0.1
9	80	0.93	5	0.210	0.1
10	90	0.82	5	0.231	0.1
11	100	0.74	5	0.252	0.1
12	125	0.59	5	0.273	0.1
13	150	0.49	5	0.294	0.1
14	175	0.42	5	0.315	0.1
15	200	0.37	5	0.336	0.1
16	225	0.33	5	0.357	0.1
17	250	0.30	5	0.378	0.1
18	275	0.27	5	0.399	0.1
19	300	0.25	5	0.420	0.1

Acknowledgements

This work is the result of collaboration across the entire QuantumScape organization. In particular, the authors wish to recognize Aditya Bitra, Josh Deetz, Niall Donnelly, Will Gardner, Wes Hermann, Tom Heuser, Hansong Huang, Sriram Iyer, Ji Maan Kim, Jon Snider, Samuel Stansell, Vikram Thridandam, Qizhong Wang, and Gengfu Xu for their input and contributions.

Author Information

Corresponding Author

*E-mail: th+jes@quantumscape.com

Notes

Conflict of Interest

The authors are employees of QuantumScape Battery, Inc., which holds financial and commercial interests in the research and development described in this article. These interests may include, but are not limited to, proprietary technologies, products, and future commercial applications related to the subject matter.

References

[1] W. Xu, J. Wang, F. Ding, X. Chen, E. Nasybulin, Y. Zhang, J.G. Zhang, Energy Environ. Sci., 7, 513 (2014).

[2] R. Schmuch, R. Wagner, G. Hörpel, T. Placke, M. Winter, Nature Energy 2018 3:4, 3, 267 (2018).

[3] T. Fuchs, C.G. Haslam, A.C. Moy, C. Lerch, T. Krauskopf, J. Sakamoto, F.H. Richter, J. Janek, Adv. Energy Mater., 12 (2022).

[4] X.B. Cheng, R. Zhang, C.Z. Zhao, Q. Zhang, Chem. Rev., 117, 10403 (2017).

[5] S. Zhang, B. Hu, Z. Geng, X. Gao, D. Spencer-Jolly, D.L.R. Melvin, Z. Ning, G. Li, M. Jenkins, L. Wang, H. Gao, S.D. Pu, T.J. Marrow, C.W. Monroe, P.G. Bruce, Energy Environ. Sci., 17, 1448 (2024).

[6] D. Cao, X. Sun, Q. Li, A. Natan, P. Xiang, H. Zhu, Matter, 3, 57 (2020).

[7] Y. Lu, C.Z. Zhao, H. Yuan, X.B. Cheng, J.Q. Huang, Q. Zhang, Adv. Funct. Mater., 31 (2021).

[8] S. Sarkar, V. Thangadurai, ACS Energy Lett., 7, 1492 (2022).

[9] D.L.R. Melvin, M. Siniscalchi, D. Spencer-Jolly, B. Hu, Z. Ning, S. Zhang, J. Bu, S. Marathe, A. Bonnin, J. Ihli, G.J. Rees, P.S. Grant, T.J. Marrow, G. Li, P.G. Bruce, High plating currents without dendrites at the lithium anode/solid electrolyte interface. ChemRxiv. (2024), doi:10.26434/chemrxiv-2024-64djb-v3

[10] F. Flatscher, M. Philipp, S. Ganschow, H.M.R. Wilkening, D. Rettenwander, J. Mater. Chem. A, 8, 15782 (2020).

[11] H. Huo, Y. Chen, R. Li, N. Zhao, J. Luo, J.G. Pereira Da Silva, R. Mücke, P. Kaghazchi, X. Guo, X. Sun, Energy Environ. Sci., 13, 127 (2020).

[12] J. Kasemchainan, S. Zekoll, D. Spencer Jolly, Z. Ning, G.O. Hartley, J. Marrow, P.G. Bruce, Nature Materials 2019 18:10, 18, 1105 (2019).

[13] L. Cheng, W. Chen, M. Kunz, K. Persson, N. Tamura, G. Chen, M. Doeff, ACS Appl. Mater. Interfaces, 7, 2073 (2015).

[14] G. Liu, W. Weng, Z. Zhang, L. Wu, J. Yang, X. Yao, Nano Lett., 20, 6660 (2020).

[15] G.T. Hitz, D.W. McOwen, L. Zhang, Z. Ma, Z. Fu, Y. Wen, Y. Gong, J. Dai, T.R. Hamann, L. Hu, E.D. Wachsman, Materials Today, 22, 50 (2019).

[16] H. Huo, Y. Chen, N. Zhao, X. Lin, J. Luo, X. Yang, Y. Liu, X. Guo, X. Sun, Nano Energy, 61, 119 (2019).

[17] Y.G. Lee, S. Fujiki, C. Jung, N. Suzuki, N. Yashiro, R. Omoda, D.S. Ko, T. Shiratsuchi, T. Sugimoto, S. Ryu, J.H. Ku, T. Watanabe, Y. Park, Y. Aihara, D. Im, I.T. Han, Nature Energy 2020 5:4, 5, 299 (2020).

[18] Y. Su, L. Ye, W. Fitzhugh, Y. Wang, E. Gil-González, I. Kim, X. Li, Energy Environ. Sci., 13, 908 (2020).

[19] T. Deng, X. Ji, Y. Zhao, L. Cao, S. Li, S. Hwang, C. Luo, P. Wang, H. Jia, X. Fan, X. Lu, D. Su, X. Sun, C. Wang, J.G. Zhang, Advanced Materials, 32, 2000030 (2020).

[20] R.J.Y. Park, C.M. Eschler, C.D. Fincher, A.F. Badel, P. Guan, M. Pharr, B.W. Sheldon, W.C. Carter, V. Viswanathan, Y.M. Chiang, Nature Energy 2021 6:3, 6, 314 (2021).

[21] S. Kim, J.S. Kim, L. Miara, Y. Wang, S.K. Jung, S.Y. Park, Z. Song, H. Kim, M. Badding, J.M. Chang, V. Roev, G. Yoon, R. Kim, J.H. Kim, K. Yoon, D. Im, K. Kang, Nature Communications 2022 13:1, 13, 1 (2022).

[22] A. Sharafi, H.M. Meyer, J. Nanda, J. Wolfenstine, J. Sakamoto, J. Power Sources, 302, 135 (2016).

[23] T. Fuchs, C.G. Haslam, F.H. Richter, J. Sakamoto, J. Janek, Adv. Energy Mater., 13 (2023).

[24] M. Yang, Y. Liu, A.M. Nolan, Y. Mo, Advanced Materials, 33, 2008081 (2021).

[25] M.J. Wang, R. Choudhury, J. Sakamoto, Joule, 3, 2165 (2019).

[26] S.Y. Ham, H. Yang, O. Nunez-cuacuas, D.H.S. Tan, Y.T. Chen, G. Deysher, A. Cronk, P. Ridley, J.M. Doux, E.A. Wu, J. Jang, Y.S. Meng, Energy Storage Mater., 55, 455 (2023).

[27] A. Tron, A. Orue, P. López-Aranguren, A. Beutl, J. Electrochem. Soc., 170, 100525 (2023).

[28] M. Klimpel, H. Zhang, M. V. Kovalenko, K. V. Kravchyk, Communications Chemistry 2023 6:1, 6, 1 (2023).

[29] J. Kasemchainan, S. Zekoll, D. Spencer Jolly, Z. Ning, G.O. Hartley, J. Marrow, P.G. Bruce, Nat. Mater., 18, 1105 (2019).

[30] S.S. Shishvan, N.A. Fleck, V.S. Deshpande, J. Power Sources, 488, 229437 (2021).

[31] J.A.B. Agier, S.S. Shishvan, N.A. Fleck, V.S. Deshpande, Acta Mater., 240, 118303 (2022).

[32] F.N. David, N.L. Johnson, Biometrika, 41, 228 (1954).

[33] T. Krauskopf, B. Mogwitz, C. Rosenbach, W.G. Zeier, J. Janek, Adv. Energy Mater., 9, 1902568 (2019).

[34] D. Spencer Jolly, Z. Ning, G.O. Hartley, B. Liu, D.L.R. Melvin, P. Adamson, J. Marrow, P.G. Bruce, ACS Appl. Mater. Interfaces, 13, 22708 (2021).

[35] T. Krauskopf, F.H. Richter, W.G. Zeier, J. Janek, Chem. Rev., 120, 7745 (2020).

[36] T. Krauskopf, H. Hartmann, W.G. Zeier, J. Janek, ACS Appl. Mater. Interfaces, 11, 14463 (2019).

[37] N.J. Taylor, S. Stangeland-Molo, C.G. Haslam, A. Sharafi, T. Thompson, M. Wang, R. Garcia-Mendez, J. Sakamoto, J. Power Sources, 396, 314 (2018).

[38] H. Zheng, S. Wu, R. Tian, Z. Xu, H. Zhu, H. Duan, H. Liu, Adv. Funct. Mater., 30, 1906189 (2020).

[39] C. Zheng, Y. Lu, Q. Chang, Z. Song, T. Xiu, J. Jin, M.E. Badding, Z. Wen, Adv. Funct. Mater., 33, 2302729 (2023).

[40] Y. Lu, X. Huang, Y. Ruan, Q. Wang, R. Kun, J. Yang, Z. Wen, J. Mater. Chem. A, 6, 18853 (2018).

[41] F. Han, J. Yue, X. Zhu, C. Wang, Adv. Energy Mater., 8, 1703644 (2018).

[42] P. Royston, M.K.B. Parmar, BMC Med. Res. Methodol., 13, 1 (2013).

[43] B. Kinzer, A.L. Davis, T. Krauskopf, H. Hartmann, W.S. LePage, E. Kazyak, J. Janek, N.P. Dasgupta, J. Sakamoto, Matter, 4, 1947 (2021).

[44] M. Wang, J.B. Wolfenstine, J. Sakamoto, Electrochim. Acta, 296, 842 (2019).

[45] C.L. Tsai, V. Roddatis, C.V. Chandran, Q. Ma, S. Uhlenbruck, M. Bram, P. Heitjans, O. Guillon, ACS Appl. Mater. Interfaces, 8, 10617 (2016).

[46] W.S. LePage, Y. Chen, E. Kazyak, K.-H. Chen, A.J. Sanchez, A. Poli, E.M. Arruda, M.D. Thouless, N.P. Dasgupta, J. Electrochem. Soc., 166, A89 (2019).

[47] W.Q. Meeker, L.A. Escobar, F.G. Pascual, Statistical Methods for Reliability Data, John Wiley & Sons (2022).

[48] J.B. Wachtman, W.R. Cannon, M.J. Matthewson, Mechanical Properties of Ceramics, Second Editon, John Wiley & Sons (2009).

[49] G. McConohy, X. Xu, T. Cui, E. Barks, S. Wang, E. Kaeli, C. Melamed, X.W. Gu, W.C. Chueh, Nature Energy 2023 8:3, 8, 241 (2023).

[50] Z. Ning, G. Li, D.L.R. Melvin, Y. Chen, J. Bu, D. Spencer-Jolly, J. Liu, B. Hu, X. Gao, J. Perera, C. Gong, S.D. Pu, S. Zhang, B. Liu, G.O. Hartley, A.J. Bodey, R.I. Todd, P.S. Grant, D.E.J. Armstrong, T.J. Marrow, C.W. Monroe, P.G. Bruce, Nature 2023 618:7964, 618, 287 (2023).

[51] A. Aryanfar, D.J. Brooks, A.J. Colussi, B. V. Merinov, W.A. Goddard, M.R. Hoffmann, Phys. Chem. Chem. Phys., 17, 8000 (2015).

[52] S. Chen, F. Dai, M. Cai, ACS Energy Lett., 5, 3140 (2020).

[53] J.Y. Hwang, S.J. Park, C.S. Yoon, Y.K. Sun, Energy Environ. Sci., 12, 2174 (2019).

[54] J. Singh, T. Holme, in Zenodo, (2020).